Author/s:
Tang, T;Jiang, WJ;Niu, S;Liu, N;Luo, H;Zhang, Q;Wen, W;Chen, YY;Huang, LB;Gao, F;Hu, JS

Title:
Kinetically Controlled Coprecipitation for General Fast Synthesis of Sandwiched Metal Hydroxide Nanosheets/Graphene Composites toward Efficient Water Splitting

Date:
2018-01-17

Citation:
Tang, T., Jiang, W. J., Niu, S., Liu, N., Luo, H., Zhang, Q., Wen, W., Chen, Y. Y., Huang, L. B., Gao, F. & Hu, J. S. (2018). Kinetically Controlled Coprecipitation for General Fast Synthesis of Sandwiched Metal Hydroxide Nanosheets/Graphene Composites toward Efficient Water Splitting. Advanced Functional Materials, 28 (3), https://doi.org/10.1002/adfm.201704594.

Persistent Link:
https://hdl.handle.net/11343/261079

DOI: 10.1002/ ((please add manuscript number))

Article type: Full Paper

Kinetically Controlled Coprecipitation for General Fast Synthesis of Sandwiched Metal Hydroxide Nanosheets/Graphene Composites towards Efficient Water Splitting

Tang Tang, Wen-Jie Jiang, Shuai Niu, Ning Liu, Hao Luo, Qiang Zhang, Wu Wen, Yu-Yun Chen, Lin-Bo Huang, Feng Gao,* Jin-Song Hu**

T. Tang, Q. Zhang, W. Wen, Prof. F. Gao

Laboratory of Functionalized Molecular Solids, Ministry of Education, Anhui Key Laboratory of Chemo/Biosensing, Laboratory of Optical Probes and Bioelectrocatalysis,

College of Chemistry and Materials Science, Anhui Normal University, Wuhu 241000, China

E-mail: fgao@mail.ahnu.edu.cn

T. Tang, Dr. W.-J. Jiang, S. Niu, H. Luo, Dr. Y.-Y. Chen, L.-B. Huang, Prof. J.-S. Hu

CAS Key Laboratory of Molecular Nanostructure and Nanotechnology, CAS Research/Education Center for Excellence in Molecular Sciences,

Institute of Chemistry, Chinese Academy of Sciences (CAS), Beijing 100190, China

E-mail: jiangwenjie@iccas.ac.cn, hujs@iccas.ac.cn

N. Liu

Research & Development Centre for Functional Crystals, Beijing National Laboratory for Condensed Matter Physics, Institute of Physics, Chinese Academy of Sciences, Beijing 100190, China

Dr. W.-J. Jiang, Prof. J.-S. Hu

School of Chemistry and Chemical Engineering,

University of the Chinese Academy of Sciences

Beijing 100049 (China)

Keywords: Hydroxide nanosheets, Kinetical control, Oxygen evolution, Sandwiched nanostructure, Water splitting

Abstract

The development of cost-effective and applicable strategies for producing efficient OER electrocatalysts is crucial to advance electrochemical water splitting. Herein, a kinetically controlled room-temperature coprecipitation was developed as a general strategy to produce a variety of sandwich-type metal hydroxide/graphene composites. Specifically, well-defined α-phase nickel cobalt hydroxides nanosheets are vertically assembled on the entire graphene surface (NiCo-HS@G) to provide plenty of accessible active sites and enable facile gas escaping. The tight contact between NiCo-HS and graphene promises effective electron transfer and remarkable durability. It is discovered that Ni doping adjusts the nanosheet morphology to augment active sites and effectively modulates the electronic structure of Co center to favor the adsorption of oxygen species. Consequently, NiCo-HS@G exhibits superior electrocatalytic activity and durability for OER with a very low overpotential of 259 mV at 10 mA/cm^2. Furthermore, a practical water electrolyzer demonstrates a small cell voltage of 1.51 V to stably achieve the current density of 10 mA/cm^2, and 1.68 V to 50 mA/cm^2. Such superior electrocatalytic performance indicates that this facile and manageable strategy with low energy consumption may open up opportunities for the cost-effective mass production of various metal hydroxides/graphene nanocomposites with desirable morphology and competing performance for diverse applications.

1. Introduction

The continuing growth of greenhouse gas emissions and public concerns about the energy crisis calls for the development of sustainable energy as viable alternatives to fossil fuels, thus the trend to

develop clean energy sources is irreversible.[1, 2] Among many energy storage technologies, electrochemical splitting water into H_2 and O_2 is considered one of the most promising way to enable the storage of renewable energies such as solar and wind.[3, 4] However, the sluggish oxygen evolution reaction (OER) kinetics at the anode greatly hindered the overall water splitting performance because of the complex four-electron oxidation process,[5-7] leading to the high electricity cost and thus limiting the practical application of this technique. Currently, the state-of-the-art catalysts for OER in electrolytic cells are still ruthenium (Ru) and iridium (Ir) oxides, which are among the rarest elements in Earth's storage.[8, 9] Therefore, it still remains challenging to search for cost-effective alternative catalysts with a potential for mass production and high activity and durability to significantly reduce the electricity consumption.

Over the last few years, various transition metal based catalysts have been intensively investigated as OER catalysts, such as metal hydr(oxy)oxides,[5, 10-13] oxides[14-19], and chalcogenides,[6, 8, 20-24] because of their large elemental abundance and low cost. Among them, metal hydroxides received quite a lot attention due to the low cost, easy preparation, as well as eco-friendly synthesis compared with metal chalcogenides and phosphides etc., but suffered from poor conductivity which limited their OER activity and the practical utilization at large output. To overcome this disadvantage, incorporating conductive materials was proved as an effective way to improve their low electron transfer ability.[25-27] Several reports have demonstrated graphene could take advantage of its high conductivity and large surface area to serve this purpose so well.[28-31] Thus, graphene/metal hydroxide composites recently have been developed mainly by hydrothermal method as promising and advanced electrode materials for electrocatalysis and supercapacitors.[32-34] Unfortunately, hydrothermal method usually delivered irregular and non-uniform products due to

the incapability in kinetical control.[35, 36] It is necessary but still challenging to develop facile and scalable approaches to produce graphene/metal hydroxide composites with controllable and desirable morphologies aiming for high electrocatalytic performance.

The electrocatalytic performance of a catalyst is determined by the quantity of accessible active site and its intrinsic activity. On one hand, catalyst morphology at nanoscale significantly influences the quantity of exposed active sites and thus the catalytic performance for water splitting.[3, 11, 37] Generally, the final product morphology depends on whether the preparation is controlled by thermodynamic or dynamic process. The nucleation and growth rates determine the product morphology and the "best-performing" morphology can thus be achieved by modulating the dominant process during the material preparation. Coprecipitation reaction under stirring is known as a promising method for mass production of composites since it is an industrial-compatible process which could occur at room temperature and be controlled in a thermodynamic or dynamic way. The competing between thermodynamic self-nucleation and dynamic diffusion of anions determines the final product morphology. The dominant process could be tuned by reaction conditions such as the stirring rate, reactant concentration, and temperature etc. For the practical application of electrocatalyst, proper conditions for coprecipitation could optimize the catalyst morphology to augment the quantity of active sites for boosting the electrocatalytic performance.[38-40] With the coprecipitation method, binary NiFe and trinary NiCoFe layered double hydroxides were synthesized as OER catalysts by Vargas's and Sun's groups,[41, 42] although the controllable synthesis of metal hydroxides, especially bimetal hydroxides on graphene via coprecipitation for OER application was rarely reported. On the other hand, the catalytic performance can be improved by enhancing the intrinsic activity of active site. As demonstrated in the previous work from our group

and others, it is found that the intrinsic activity of active site could be boosted by optimizing the electronic structure of active center via the interaction with other elements[10, 14, 43-45]. Combining these strategies together, it would be possible to explore the graphene/metal hydroxide composites with controllable morphology to achieve the superior electrocatalytic performance.

Inspired by the above discussion, we herein developed a general, fast, one-step strategy to prepare sandwiched metal hydroxide/graphene composites with the morphology of well-defined hydroxide nanosheet array on graphene layer through a kinetically controlled coprecipitation under room temperature. This strategy is eco-friendly, low energy-consuming and compatible with industrial scale. Besides the general synthesis of a wide range of single metal hydroxide composites, such approach also allows to produce bimetal hydroxides to delicately modulate the electronic structure of metal center for further boosting the electrocatalytic performance of composites. For example, it was found that well-defined Ni-doped $Co(OH)_2$ nanosheets vertically assembled on graphene matrix to an oriented sandwich-type composite (denoted as NiCo-HS@G) could be reproducibly produced in a large scale. Such NiCo-HS@G exhibited superior electrocatalytic performance for OER with an small overpotential of 302 mV at 10 mA cm^{-2}, 373 mV at 100 mA cm^{-2}, and a Tafel slope of 49.6 mV dec^{-1}, much lower than those for reported Co-based materials[10, 21, 30]. Furthermore, a three-dimensional NiCo-HS@G architecture on nickel foam (NiCo-HS@G/NF) electrode were further fabricated to deliver 10 mA cm^{-2} at 259 mV for OER. The overall water electrolyzer configured with NiCo-HS@G/NF anode and NiMo electrodeposited NiCo-HS@G/NF cathode demonstrated a small cell voltage of 1.51 V and 1.68 V at 10 and 50 mA cm^{-2}, respectively. Such superior catalytic performance enables the potential application of novel NiCo-HS@G composites in practical water electrolysis. In view of the facile and manageable processing of the

present strategy with low energy consumption, these findings inspire the mass production of a variety of metal hydroxides/graphene composites with desirable morphology and competing performance for diverse energy applications.

2. RESULTS AND DISCUSSION

As shown in Scheme 1, the sandwich-type Co, Ni, or Co-Ni hydroxides/graphene composites with well-defined morphology was successfully synthesized via a simple one-step kinetically controlled coprecipitation at room temperature (details seen in Experimental Section). The metal cations adsorbed on the defects of graphene layer was supposed to act as nucleation sites. The high-speed stirring was used to control the growth kinetics of hydroxides and accelerate the cations diffusion to form uniform well-defined morphology. The coprecipitation process can be done in 5 min. The prepared Ni-HS@G, Co-HS@G and bimetallic NiCo-HS@G products showed the dark, light greenish-blue, and light bluish-green color, respectively (Figure S1). For comparison, bimetal NiCo-HS was also prepared with the same procedure except for without addition of graphene as matrix and shows a brown color.

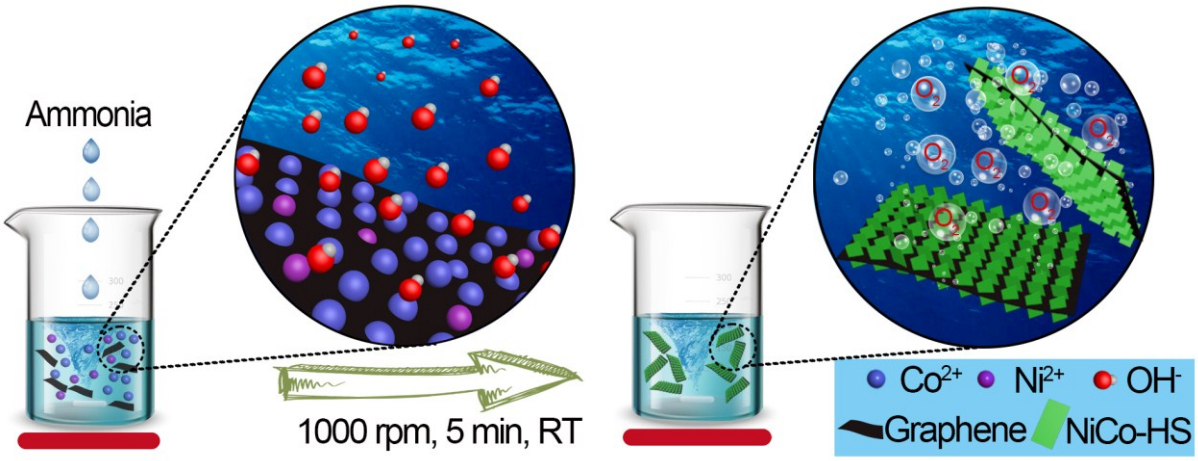

Scheme 1. Schematic illustration of the fabrication process of NiCo-HS@G.

X-ray diffraction (XRD) technique was used to investigate the crystalline phase and composition of these materials (Figure 1a). XRD pattern of Ni-HS@G can be attributed to hexagonal β-$Ni(OH)_2$ (JCPDS No. 14-0117), except for the diffraction peak at 26.3° marked by pink asterisk, which can be indexed to the (002) planes of graphene (JCPDS No. 41-1487). The diffraction peaks in the XRD pattern of Co-HS@G at 10.2°, 20.4°, 34.4°, and 60.7° can be well indexed to the (003), (006), (101), and (110) planes of hexagonal α-$Co(OH)_2$ (JCPDS No. 30-0443), respectively. No graphene peaks were clearly observed in these XRD patterns, implying the hydroxide nanosheets densely wrapped the graphene layers. Since previous reports demonstrated that α-phase nickel hydroxide exhibited superior OER activity to β-phase one,[46]

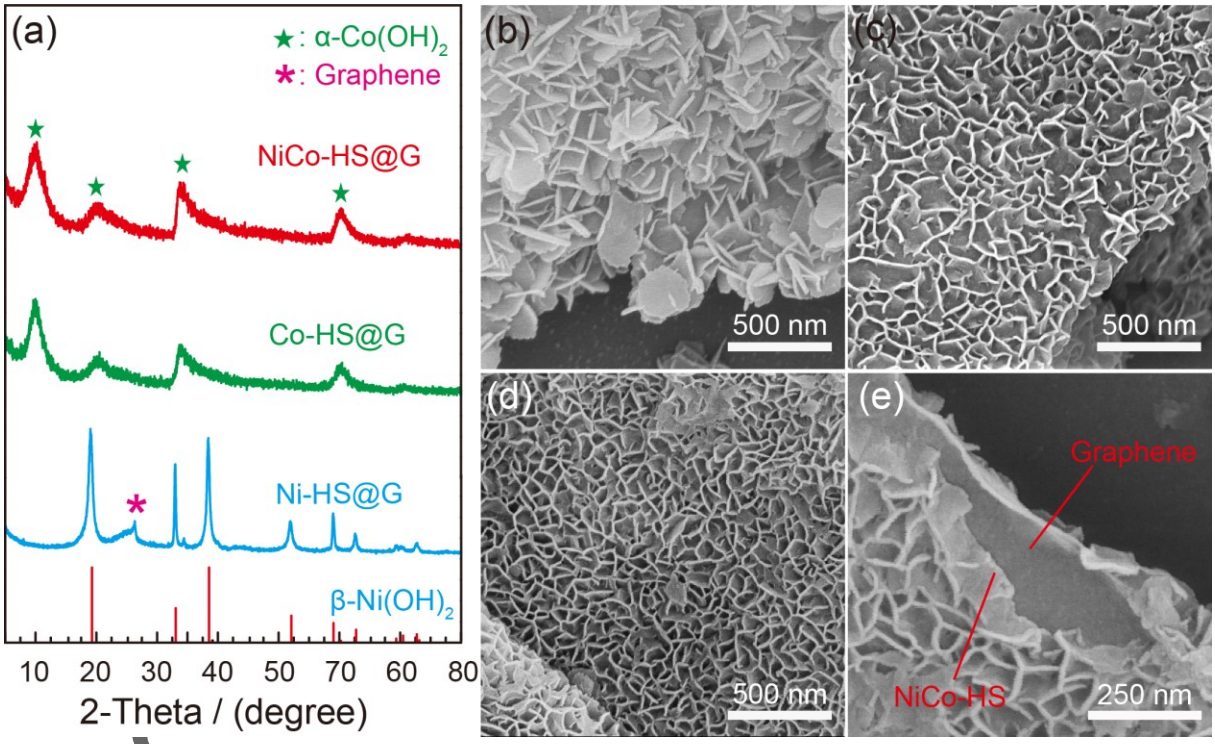

Figure 1. (a) XRD patterns of Ni-HS@G, Co-HS@G and NiCo-HS@G. The peaks marked by asterisk, pentacle symbol and are indexed to graphene (JCPDS No. 41-1487) and α-$Co(OH)_2$ (JCPDS No. 30-0443), respectively. The vertical lines are indexed to β-$Ni(OH)_2$ (JCPDS No. 14-0117). SEM images of (b) Ni-HS@G, (c) Co-HS@G, (d) NiCo-HS@G. (e) Zoom-in SEM image of NiCo-HS@G after ultrasonic treatment.

we selected Ni as doping element to achieve α-phase bimetallic Ni,Co-hydroxides for investigating the effect of electronic modulation by secondary metal on the electrocatalytic performance. The prepared NiCo-HS@G showed the XRD patterns similar to pure Co-HS@G (Figure 1a), indicating their crystalline structure could be attributed to hexagonal α-$Co(OH)_2$ which is preferable for electrocatalytic oxygen evolution. The morphology of these samples were investigated by scanning electron microscopy (SEM) as provided in Figure 1b-e. The Ni-HS@G showed that irregular hydroxide nanosheets randomly stacked and partially covered on the graphene surface (Figure 1b). In contrast,

the hydroxide nanosheets became aligning on the graphene layer to form an interconnected nanowall-like structure for Co-HS@G (Figure 1c). After introducing Ni component, NiCo-HS@G reserved the morphology of Co-HS@G (Figure 1d) but with higher density of nanosheets in a smaller size. The thickness of nanosheet is around 3 nm and the size is around 45 nm. The low-magnification SEM images showed that all graphene layers were uniformly sandwiched by such nanosheet network (Figure S2a). These nanosheets interconnected together to form a film with 3D open structure on each side of graphene layers (Figure S2b). No naked graphene layers without metal hydroxide nanosheets or self-nucleated metal hydroxide nanosheets without graphene layers were observed, indicating the present approach of room-temperature coprecipitation under high-speed stirring is highly effective to achieve the sandwich-type vertically-aligned hydroxide nanosheets/graphene composites. In order to inspect the interface between the nanosheets and graphene layer, NiCo-HS@G sample was subjected to an intense ultrasonic treatment to intentionally break the sandwiched structure. A zoom-in observation on a rarely-seen broken edge clearly revealed that NiCo-HS were tightly grown on both sides of the graphene layer (Figure 1e). Such hierarchal structure not only effectively prevented the agglomeration of graphene layers and offered large surface area for exposing more electrocatalytically active sites, but also facilitated the gas evolution and detachment through the vertically aligned nanowall-like structure with open interspaces. The interconnection of these nanosheets also enhanced the structure stability and the intimate contact between the nanosheets and graphene layers, guarantying the efficient electron transfer and high durability during electrochemical operation.[40, 47, 48]

The morphology and structure of NiCo-HS@G were further investigated by transmission electron microscopy (TEM). TEM image in Figure 2a corroborates that plenty of nanosheets vertically grow

on the surface of graphene matrix. The zoom-in TEM image in Figure 2b indicates that the thickness of nanosheet is around 3 nm, consistent with SEM result. The continuous lattice fringes with a distance of 0.779 nm (Figure 2b) can be indexed to the *d* spacing of (003) planes of α-$Co(OH)_2$ phase. The homogeneous doping of elemental Ni in NiCo-HS@G is proven by energy dispersive spectroscopy (EDS) mapping results as shown in Figure 2c-g. The atomic ratio of Co to Ni is determined to be about 4:1 (Figure S3). It is interestingly noted that this ratio and the morphology of NiCo-HS@G are independent on the feeding ratio of Co:Ni. Even the feeding ratio of Co:Ni was changed from 2:1 to 1:9 or 9:1, the Co:Ni ratio of in the final product maintained at about 4:1 and the sandwiched morphology of hydroxide nanosheets on graphene was not changed (Figure S4).

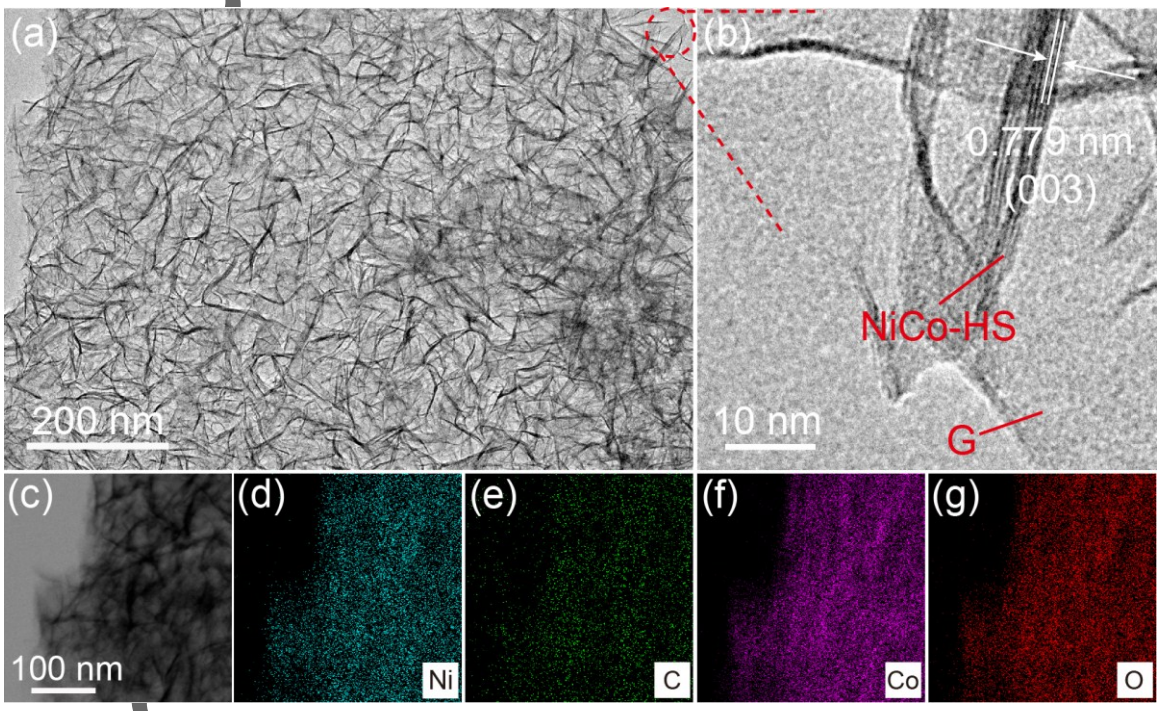

Figure 2. (a) TEM image, (b) the enlarged TEM image of selected area in (a), and (c-g) EDS mapping of NiCo-HS@G.

Above results demonstrate the success in the uniform incorporation of NiCo-HS on graphite matrix to achieve NiCo-HS@G composites by the developed kinetically-controlled coprecipitation method. In order to demonstrate the advantage of this coprecipitation method, the hydrothermal processing without stirring, which was commonly used in the literatures to obtain the graphene-based composite, was also applied to synthesize the composites of metal hydroxide and graphene (details seen in Experimental Section). Unfortunately, it was found that when the temperature was elevated to 50 ^{o}C, the graphene aggregates showed up and

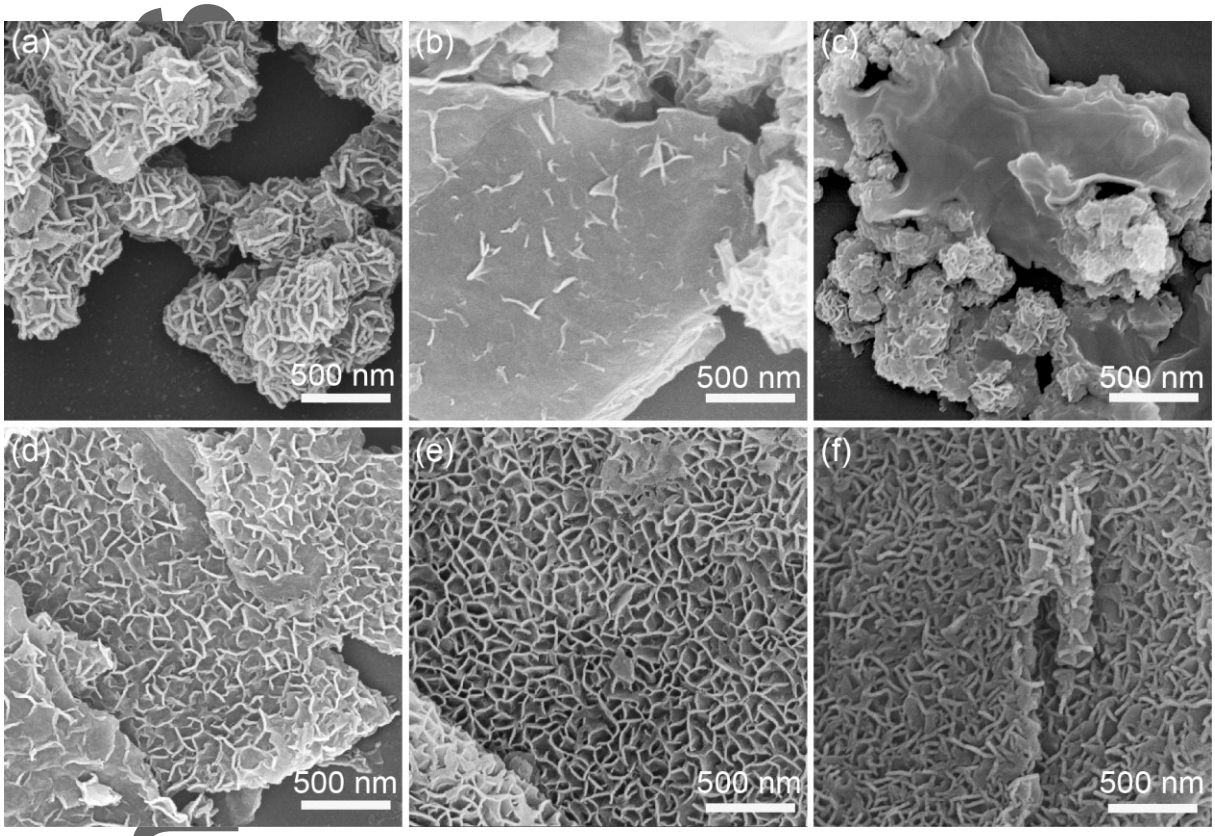

Figure 3. SEM images of NiCo-HS@G composites synthesized under different stirring rates of (a) 100, (b) 300, (c) 500, (d) 700, (e) 1000, (f) 1200 rpm.

metal hydroxides could not effectively grow on the graphene layers, so the products obtained under hydrothermal condition without the stirring are composed of irregular nanosheets-assembled particles (Figure S5). To further understand the formation process of the sandwiched NiCo-HS@G, the role of graphene and the effect of stirring rate on the product morphology was investigated. The counterpart without the addition of graphene (NiCo-HS) was also prepared and its XRD pattern (Figure S6a) shows the diffraction peaks of α-$Co(OH)_2$, which is the same with NiCo-HS@G. As shown in Figure S6b, without the graphene skeleton, hydroxide nanosheets self-nucleated and assembled into irregular particles in a size of hundreds of nanometers. It is known that the final morphology of a nanomaterial depends on its nucleation and growth process. In our case, the morphology of the present NiCo-HS@G composite is supposed to be determined by where the initial nucleation of hydroxides occurs and the competition between self-nucleation and hydroxides growth, which can be affected by the mass transportation. If the NiCo-HS initially nucleates onto the graphene layer, the well-defined NiCo-HS@G composite could be achieved by controlling the following growth process while avoiding the self-nucleation process. In our experiments, it was found that the self-nucleated products with the morphology of irregular nanosheets-assembled particles were always obtained without the stirring or under a stirring rate of 100 rpm (Figure 3a), like that prepared via hydrothermal processing without stirring (Figure S5). Increasing stirring rate to 300 and 500 rpm, hydroxide nanosheets started to grow on the graphene matrix (Figure 3b-c) but still an appreciable amount of graphene layers were not covered by hydroxides. When the stirring rate was further increased to 700 rpm, almost all graphene substrates were covered by hydroxide nanosheets and self-nucleated particles were seldom observed (Figure 3d). The sandwiched structure with well-aligned hydroxide nanosheets on graphene was achieved at a stirring rate of 1000 rpm (Figure 3e). The density of nanosheets on graphene became higher if keeping increasing the rate to 1200 rpm (Figure 3f). These observations indicate that the stirring rate during coprecipitation process significantly influences the thermodynamic self-

nucleation and dynamic diffusion controlled growth process. Since the graphene layers with some degree of oxidation contain abundant carbonyl and carboxyl groups, the metal cations will adsorb on the graphene which will initialize the heterogeneous nucleation of metal hydroxides upon the addition of ammonia aqueous solution. The high stirring rate promises the instant mass transportation for the growth of these hydroxide nuclei instead of the formation of new nucleus via self-nucleation of reactants, leading to the well-defined sandwiched Ni/Co-HS@G composite. In contrast, the low stirring rate causes the insufficient mass transportation and thus the accumulation of reactant ions to initialize the homogeneous self-nucleation, followed by the growth of all kinds of nuclei, resulting in the self-seeded hydroxide particles. Based on the above understanding, this kinetically controlled heterogeneous nucleation and precipitation strategy should work as a versatile method for the synthesis of other metal hydroxide/graphene composites. To prove this hypothesis, the strategy was extended to prepare a series of composites with metal hydroxides grown on graphene layers by using different metal cations instead of Ni or Co. As shown in Figure S7, Mg, Al, Cr, Mn, Fe, Cu, Zn, and Zr hydroxide nanostructures can be selectively grown onto the both sides of graphene layer matrix without the detectable self-nucleated growth. Depending on the crystal habits, Al, Cr, Mn, and Zr hydroxides tend to form nanoparticles while Mg, Fe, Cu, and Zn hydroxides prefer to form nanosheets.

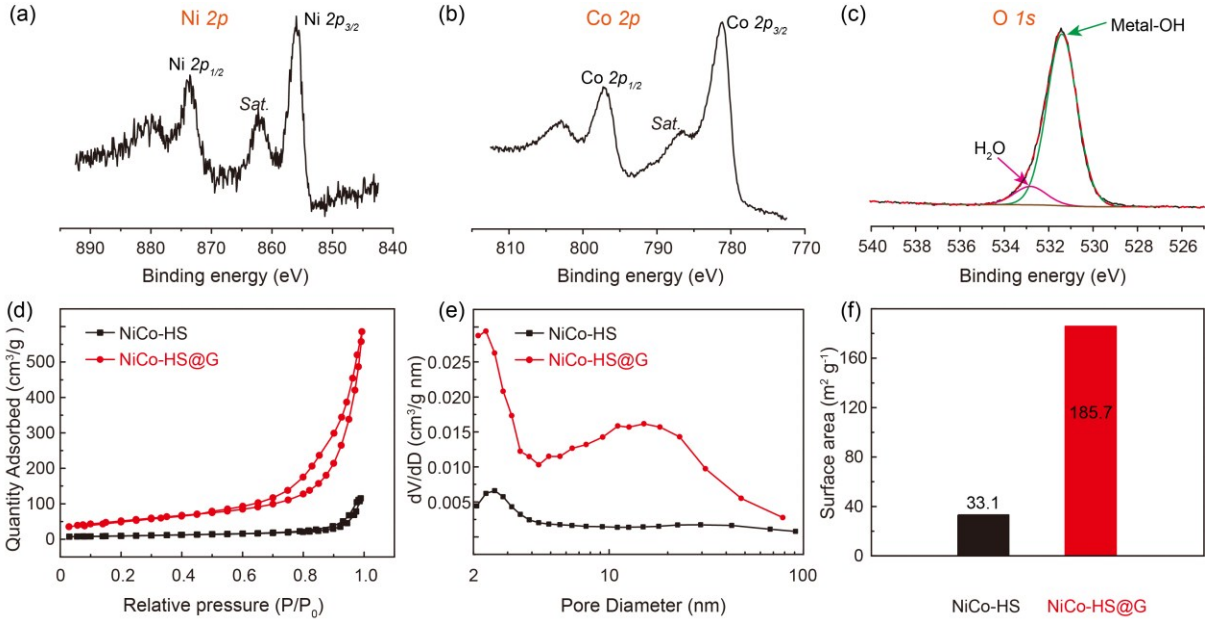

Figure 4. XPS spectra of (a) Ni 2*p*, (b) Co 2*p*, and (c) O *1s* for Ni-Co-HS@G. (d) N_2 adsorption/desorption isotherms, (e) Pore size distribution curves, and (f) surface areas of NiCo-HS and NiCo-HS@G.

The composition and elemental chemical states of NiCo-HS@G were monitored by X-ray photoelectron spectroscopy (XPS). The Ni $2p_{3/2}$ (Figure 4a) spectrum shows a peak at 856.1 eV, which is assigned to Ni^{2+} in $Ni(OH)_2$.[40, 49] Similarly, the Co $2p_{3/2}$ spectrum (Figure 4b) exhibits the Co^{2+} peak at 781.3 eV.[39, 50] The Co and Ni atomic percentage are measured to be 12% and 3%, respectively, giving a Co-to-Ni ratio of about 4, consistent with EDS results. O *1s* spectrum in Figure 4c shows a typical feature at 531.4 eV, which could be well indexed to metal-OH bonds in metal hydroxides. The peak located at 532.8 eV can be attributed to the adsorbed H_2O molecules.[51] These results corroborate that the composition of bimetal NiCo hydroxides. The C *1s* for NiCo-HS@G was also measured and deconvoluted as shown in Figure S8a. The peak at 284.8 eV is indexed to C = C bond from graphene layers. The peaks at 286.4, 288.1, and 298.3 eV could be assigned to C-OH, C-OOH, and O-C=O bonds, respectively, which originate from the abundant carbonyl or carboxyl

groups on graphene surface in view of that the purchased graphene were produced by the chemical methods and used as received. These functional groups could effectively anchor metal cations as nucleation sites. In addition, Raman spectrum of NiCo-HS@G was recorded to explore the surface properties of NiCo-HS@G as shown in Figure S8b. The two major peaks at 1341.8 and 1574.6 cm^{-1} are the characteristic peaks of D- and G-band of graphene, respectively. Another two minor peaks at 459.4 and 529.0 cm^{-1} could be attributed to Ni-OH and Co-OH respectively, confirming the formation of metal hydroxides.[52] Furthermore, the BET surface area and pore distribution of NiCo-HS@G were further investigated and compared with NiCo-HS. A distinct hysteresis loop in N_2 adsorption/desorption isotherm of NiCo-HS@G (red line in Figure 4e) indicates the existence of a typical mesoporous microstructure.[53, 54] While NiCo-HS (black line in Figure 4e) showed much smaller adsorption compared with NiCo-HS@G. The pore size distribution of NiCo-HS (Figure 4f) displays the nanopores centered at 2.08-2.57 nm and the mesopores ranging from 10-30 nm, which could be from the vertical nanosheet-surrounded pores. Such bimodal porous structure provides a lager specific surface area of 185.7 $m^2 g^{-1}$ for NiCo-HS@G, about 5.6 times higher than 33.1 $m^2 g^{-1}$ for NiCo-HS. This result demonstrates the critical role of graphene matrix for vertically aligning metal hydroxide nanosheets. The higher surface area with bimodal mesopores for NiCo-HS@G would provide more accessible active sites and facilitate the mass transportation of reactants and products, thus benefiting the catalytic performance.[55, 56]

To evaluate the catalytic performance of as-prepared catalysts, the electrochemical surface area (ECSA) and roughness factor (RF) were first measured by determining the double-layer capacitance (C_{dl}) (Figure S9-S10).[44] The ECSA and RF values for each catalyst are summarized in Figure 5a. The ECSA values for NiCo-HS@G, NiCo-HS, Ni-HS@G, Co-HS@G, and bare graphene were 174.9, 51.5, 4.1, 46.2 and 0.8 cm^2, respectively. The ECSA

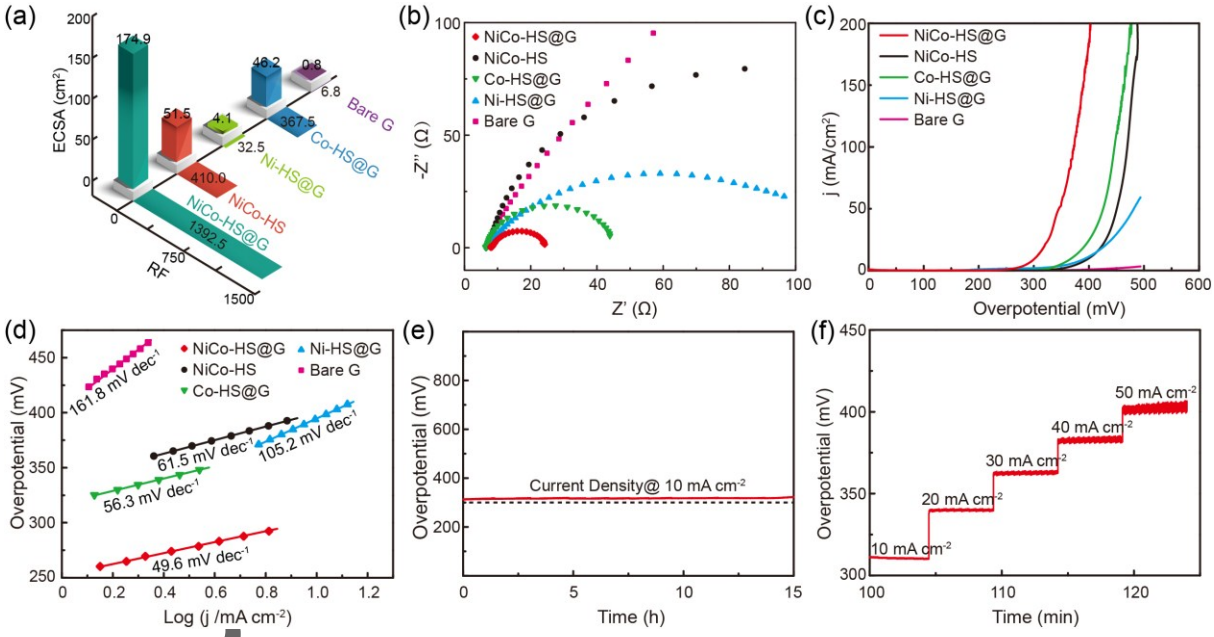

Figure 5. (a) ECSA and RF values, (b) EIS Nyquist plots at 1.53 V (*vs.* RHE), (c) OER polarization curves with 90% iR-compensation, and (d) Tafel plots of NiCo-HS@G, NiCo-HS, Ni-HS@G, Co-HS@G and bare graphene. (e) Chronopotentiometric curve at a constant current density of 10 mA cm^{-2}. (f) Multicurrent Chronopotentiometry of NiCo HNS@G for OER with current densities from 10-50 mA cm^{-2} at current ramps of 10 mA cm^{-2} per 5 min.

of NiCo-HS@G is about 218 times higher than that for bare graphene due to the introduction of hydroxide nanosheets. It is notable that the ECSA of NiCo-HS@G is almost 4 times higher than that for Co-HS@G due to the shrunk nanosheet size, indicating Ni doping could effectively modulate the morphology of Co-HS@G. The corresponding RF value of 1392.5 for Ni-Co-HS@G is the highest among all as-prepared materials, implying the largest amount of accessible active sites. Electrochemical impedance spectroscopy (EIS) technique was further used to investigate the electron transfer kinetics during OER process as shown in Figure 5b and Figure S11. All the as-prepared catalysts exhibit the similar solution resistance (R_s) of 7.2 Ω, but a significantly distinct charge transfer resistances (R_{ct}). The NiCo-HS@G catalyst shows the smallest R_{ct} value of about 16 Ω among

the values of 170 Ω for NiCo-HS, 200 Ω for Ni-HS@G, 36 Ω for Co-HS@G, and 1078 Ω for bare graphene, indicating the fastest electron transfer kinetics. To further investigate the effect of graphene skeleton on the charge-transfer process, a four-probe resistance measurement was carried to measure the powder electronic conductivity of NiCo-HS and NiCo-HS@G. The NiCo-HS@G exhibits a conductivity of 4.7×10^{-4} S cm^{-1}, which is 2 orders of magnitude higher than 6.9×10^{-6} S cm^{-1} of NiCo-HS. Such increase in the conductivity would facilitate the electron transfer during OER, thus enhancing its electrochemical activity.

The catalytic activities of as-prepared catalysts for OER were evaluated in 1 M KOH by recording linear sweep voltammetry (LSV) curves at a scan rate of 5 mV s^{-1} with 90% iR-compensation, as shown in Figure 5c. It is well known that the overpotential required to achieve the current density of 10 mA cm^{-2} is a concerned parameter for evaluating OER performance.[57] Bare graphene skeleton displays a negligible activity, indicating it is almost inactive for OER. Remarkably, NiCo-HS@G delivers such a current density of 10 mA cm^{-2} at a low overpotential of 302 mV, which is much smaller than those of NiCo-HS (399 mV), Co-HS@G (376 mV), Ni-HS@G (394 mV), and commercial benchmark IrO_2 catalyst (319 mV, Figure S12). Moreover, NiCo-HS@G could deliver the current density of 50 and 100 mA cm^{-2} at a lower overpotential of 347 mV and 373 mV, respectively, comparable to those achieved by the most active powder catalysts reported recently (Table S1).[5, 10-13, 19, 23, 24, 30, 58] LSV curves without iR-compensation were also recorded as shown in Figure S13 and exhibit the same trend of catalytic activity. The reaction kinetics of as-prepared catalysts for OER were assessed by Tafel plots as shown in Figure 5d. The NiCo-HS@G exhibits a small Tafel slope of 49.6 mV dec^{-1}, which is considerably lower than those for Co-HS@G (56.3 mV dec^{-1}), NiCo-HS (61.5 mV dec^{-1}), Ni-HS@G (105.2 mV dec^{-1}), and bare graphene (161.8 mV dec^{-1}). This result further confirmed the superior catalytic activity of NiCo-HS@G for OER. The long-term

durability of NiCo-HS@G for OER in 1 M KOH was measured at a fixed current density of 10 mA cm^{-2}. In Figure 5e, the overpotential only increases by 7 mV after continuous operation for 15 h, suggesting its excellent durability. A multicurrent step chronopotentiometry was also carried out to further evaluate the durability at various current densities. With an increment of current density at 10 mA cm^{-2} per 5 min, the change of applied overpotentials was profiled in Figure 5f. The potential keeps constant at each step under elevated *j* up to 50 mA cm^{-2}, indicating the excellent durability of the catalyst even under extremely high O_2 evolution rates. Such superior electrocatalytic performance for OER should be ascribed to the following features in NiCo-HS@G: (1) 3D vertically aligned and interconnected nanosheet arrays with open interspaces for exposing a large number of accessible active sites and efficient mass transfer, (2) the enhanced intrinsic activity of each active sites by Ni doping compared with that in Co-HS@G, and (3) the sandwich-type structure with incorporated graphene matrix for facilitating electron transfer, and (4) the tight contact between graphene and metal hydroxide nanosheets.

To explore any difference in the morphology and chemical composition of NiCo-HS@G after durability test (denoted as NiCo-HS@G-ADT), SEM and XPS characterizations were further performed after the test. As shown in the SEM image (Figure S14a), it is clear that the sandwiched structure and the interconnected nanosheets were well maintained, indicating the excellent stability. The Co *2p*, Ni *2p*, and O *1s* spectra of NiCo-HS@G-ADT were provided in Figure S14b-d. The Co $2p_{3/2}$ spectrum of NiCo-HS@G-ADT (Figure S14b) exhibits a higher shake-up peak at 790.5 eV than 786.5 eV for NiCo-HS@G, implying the formation of Co^{3+} after durability test.[59] This result was further corroborated by the negatively shifted peak for Co 2p from 781.3 eV to 779.9 eV after durability test.[60-62] The Ni $2p_{3/2}$ spectrum for NiCo-HS@G-ADT is almost same as that for NiCo-HS@G (Figure S14c), indicating the chemical valence of Ni in NiCo-HS@G remains unchanged after

durability test. It should be noted that a new peak at 528.7 eV in O *1s* spectrum of NiCo-HS@G-ADT shows up compared with that of NiCo-HS@G (Figure S14d), suggesting the slightly evolution of oxide-like environment in NiCo-HS@G-ADT.[63, 64]

To further explore the origin of better electrocatalytic activity of NiCo-HS@G than other control catalysts for OER, the chemical states of Ni or Co in Ni-HS@G and Co-HS@G counterparts were examined and compared with that in NiCo-HS@G. As shown in Figure 6a,

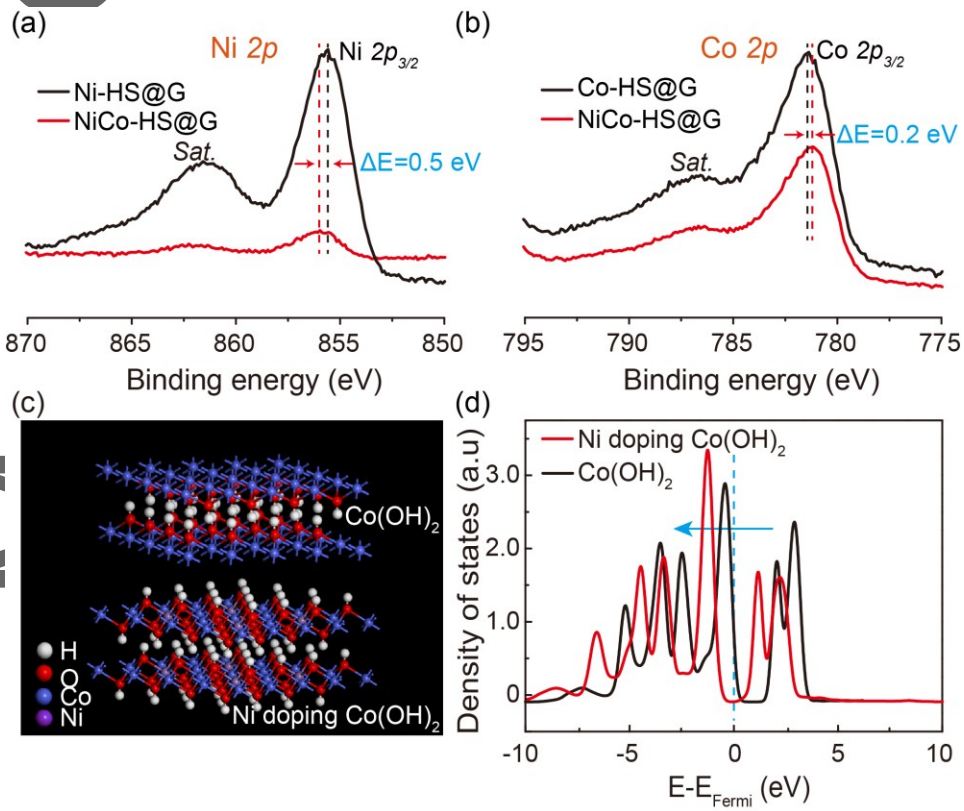

Figure 6. a) Ni $2p_{3/2}$ spectra of Ni-HS@G and NiCo-HS@G, b) Co $2p_{3/2}$ spectra of Co-HS@G and NiCo-HS@G, c) Crystal structure and d) DOS of Co 3d orbital of $Co(OH)_2$ and Ni doping $Co(OH)_2$.

the Ni^{2+} peak at 855.6 eV in NiCo-HS@G was 0.5 eV higher than that in Ni-HS@G (856.1 eV), indicating the increased oxidation state of Ni in NiCo-HS@G. On the contrary, Figure 6b displays

that the peak of Co^{2+} shifts to a lower binding energy from 781.5 eV for NiCo-HS@G to 781.3 eV for Co-HS@G, indicating the decreased oxidation sates of Co in NiCo-HS@G. These results suggest the partial electron transfer from Ni^{2+} to Co^{2+}. Considering the much lower catalytic activity of monometallic Ni-HS@G than Co-HS@G, the high activity of NiCo-HS@G should be attributed to such electronic modulation of Co by Ni doping, thus enhancing the intrinsic catalytic activity of Co.[65] Theoretical calculation on the density of states (DOS) for metal atoms was employed to understand the electronic interaction between Co and Ni in NiCo-HS@G. The optimized crystal structures of $Co(OH)_2$ and Ni-doped $Co(OH)_2$ (1/4 Co was replaced by Ni based on the atomic ratio in the NiCo-HS@G) were shown in Figure 6c. The Femi level of Co negatively shifts after Ni doping (Figure 6d), indicating Ni dopant lowers the energy of Co which allows Co to gain more electrons from Ni atoms. This theoretical result agrees with XPS measurements. Based on the previous reports, the lowered energy of Co atoms favours the formation of adsorbed OOH species, thus enhancing the OER activity.[8, 21]

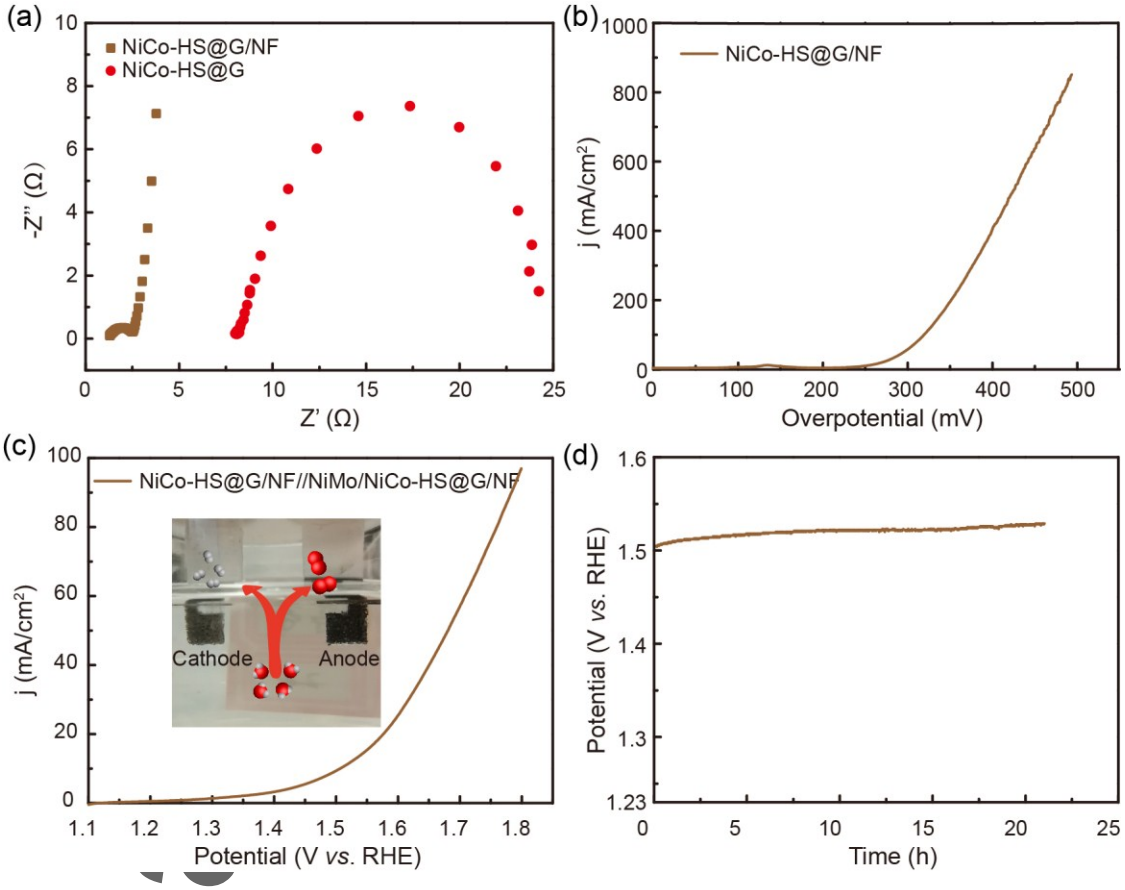

Figure 7. (a) EIS Nyquist plots at 1.53 V (*vs.* RHE) of NiCo-HS@G and NiCo-HS@G/NF. (b) OER polarization curve with 90% iR-compensation of NiCo-HS@G/NF. (c) LSV polarization curve (without iR-compensation) of NiCo-HS@G/NF//NiMo/NiCo-HS@G/NF for overall water splitting at a scan rate 5 mV s^{-1} The inset is an optical photograph of the two-electrode water electrolyzer during the measurements). (d) Long-term durability of overall water splitting at a current density of 10 mA cm^{-2}.

To take full advantage of NiCo-HS@G composites, NiCo-HS@G was deposited onto a 3D conductive nickel foam (NiCo-HS@G/NF) by ultrasonic spray coating. The EIS Nyquist plots at 1.53 V (vs. RHE) in Figure 7a indicates that both R_s (1.29 Ω) and R_{ct} (1.25 Ω) values for NiCo-HS@G/NF were significantly reduced compared with 8.08 (R_s) and 16.16 Ω (R_{ct}) for NiCo-HS@G. Notably, the Nyquist plots of NiCo-HS@G/NF exhibits a linear plot in the lower frequency region, indicating OER on NiCo-HS@G/NF is controlled by the mass transportation rather than the reaction kinetics on

NiCo-HS@G.[11] This could be aroused by the greatly enhanced charge transfer from highly conductive NF. As expected, the electrocatalytic activity of NiCo-HS@G/NF is largely enhanced in terms of a lower overpotential of 259 mV at 10 mA cm^{-2} (Figure 7b), while the OER activity of NF is negligible (Figure S15). It is worthy of noting that NiCo-HS@G/NF outputs the current densities of 50, 100, and 500 mA cm^{-2} at a very low overpotential of 295, 318, and 420 mV, respectively. Such superior OER performance inspires us to assemble an overall water splitting electrolyzer using NiCo-HS@G/NF as anode. The cathode was fabricated by simply electrodeposited NiMo alloy on NiCo-HS@G/NF (noted as NiMo/NiCo-HS@G/NF) according to our previous report.[66] NiMo/NiCo-HS@G/NF requires a very low overpotential of 51 mV to deliver 10 mA cm^{-2} for HER (Figure S16). The optical photograph of two-electrode water electrolyzer during the measurement is shown in the inset of Figure 7c, where the right electrode is the anode for O_2 production and the left one is the cathode for H_2 production. A demo video for water electrolysis is shown in Movie S1, showing the continuous gas evolution. This electrolyzer exhibits superb performance in 1 M KOH in terms of a small cell voltage of 1.51 and 1.68 V without iR-compensation to deliver 10 and 50 mA cm^{-2} (Figure 7c). This small voltage is in leading position in most of reported water electrolyzer (Table S2).[19, 37, 45, 66-73] The durability test reveals that the electrolytic voltage at 10 mA cm^{-2} shows negligible increase after continuous operation for 20 h, suggesting its good durability (Figure 7d).

3. Conclusion

In summary, we have developed a fast, one-step strategy as a versatile method to prepare a series of sandwiched metal hydroxide/graphene composites through a kinetically controlled coprecipitation under room temperature. The systematic investigation on the formation of the composite revealed that the high-speed dynamic diffusion of ions facilitates the heterogeneous

nucleation and growth of metal hydroxides while inhibits their self-nucleation. Thus, bimetallic α-phase nickel cobalt hydroxides nanosheets (NiCo-HS) can be vertically and tightly assembled on both sides of graphene matrix (NiCo-HS@G) to deliver a well-defined and stable nanostructure which is preferable for electrocatalytic application. Such NiCo-HS@G nanocomposite exhibits a superior electrocatalytic activity for OER with a small overpotential of 302 mV at 10 mA cm^{-2} and a Tafel slope of 49.6 mV dec^{-1}, which could be further improved to 259 mV by depositing NiCo-HS@G onto the nickel foam. This performance is superior to most of the reported OER catalysts, which could be ascribed to the following features: 1) The inner graphene sheet skeleton serves as a highly conductive matrix with large surface area for efficient electron transportation and high loading of active components. 2) The well-defined vertically aligned nanosheets not only offer a high electrochemically active surface area for exposing plenty of active sites but also make them accessible for reactants and benefit the gas escaping so as to guarantee the efficient mass transfer. 3) The tight contact between NiCo-HS and graphene matrix promises the effective electron transfer and remarkable durability. 4) The electronic modulation of Co center by Ni doping effectively favors the adsorption/desorption of oxygen species and thus promotes OER process. Furthermore, a water electrolyzer for overall water splitting with excellent durability was demonstrated, which output a cell voltage of 1.51 V and 1.68 V at 10 and 50 mA cm^{-2}, respectively. Such performance and the facile preparation of NiCo-HS@G opens up a new avenue for the cost-effective and low-energy-consumption production of various sandwiched metal hydroxides/graphene composites as efficient OER electrocatalysts with desired morphology and competing performance for the applications in diverse energy devices.

4. Experimental Section

Chemicals and Materials: $MgSO_4 \cdot 7H_2O$ (98%), $Al_2(SO_4)_3$ hydrate (98%), $Cr_2(SO_4)_3$ hydrate (reagent grade), $MnSO_4 \cdot H_2O$ (98%), $FeSO_4 \cdot 7H_2O$ (98%), $NiSO_4 \cdot 6H_2O$ (98%), $CoSO_4 \cdot 7H_2O$ (98%), $CuSO_4 \cdot 5H_2O$ (98%), $ZnSO_4 \cdot 7H_2O$ (98%), $ZrSO_4 \cdot 4H_2O$ (98%), Iridium (IV) oxide (99.99%), $Na_3C_6H_5O_7 \cdot 2H_2O$ (sodium citrate, 99%), and Na_2MoO_4 (sodium molybdate, 99%) were purchased from Alfa Aesar. Graphene was purchased from Nanjing XFNANO Materials Tech Co., Ltd (XFNANO). Nafion (5 wt%, DuPont) was purchased from commercial suppliers. Ethanol, ammonia aqueous solution (25-28%), hydrochloric acid, and potassium hydroxide were purchased from Beijing Chemical Work in analytic grade (A.R.). Nickel foams (NFs) (1.8 mm in thickness, 2 × 4 cm in size) were used to prepare electrodes for water electrolyzer. In order to remove the oxidation layer on surface, NFs were ultrasonically washed with a mixture solution of ethanol and acetone (1:1 in volume) for 30 minutes, followed by sonicating in HCl solution (3 M) for 15 minutes, washing with water and ethanol, and dried in air for use. All chemicals were used as received without any further purification. Milli-Q ultrapure water (resistance of 18.2 MΩ·cm at 25 °C) were used for all experiments.

Preparation of NiCo-HS@G: NiCo-HS@G was synthesized via a simple coprecipitation reaction at room temperature. First, 20 mg graphene nanosheets were ultrasonicated in 20 mL water for 10 h as solution A. 5 mmol $NiSO_4 \cdot 6H_2O$ and 10 mmol $CoSO_4 \cdot 7H_2O$ were dissolved in 30 mL water as solution B. Then, fresh-made solution A and B were mixed together under vigorous stirring (1000 rpm) to form a dark red solution. Finally, upon the drop-by-drop addition of 5 mL ammonia aqueous (25-28%), a light bluish-green precipitate formed immediately. After stirring for another 5 min, the product was collected by centrifuging, washing with water and ethanol, and then dried in a vacuum oven under 60 °C overnight.

Preparation of other metal hydroxide/graphene composites: A series of metal hydroxide/graphene composites were prepared according to the same protocol as that for NiCo-HS@G except for using the same amount of the corresponding metal salts instead. Specifically, Magnesium sulfate, Aluminum sulfate, Chromium (III) sulfate, Manganese (II) sulfate, Iron (II) sulfate, Copper (II) sulfate, Zinc sulfate and Zirconium (IV) sulfate were used for the synthesis of other metal hydroxide/graphene composites.

Preparation of the composites of Co-Ni hydroxide and graphene by hydrothermal method: In a typical hydrothermal method, urea was used as pH value regulator and structure-directing agent to form hydroxide. 1 mmol $NiSO_4 \cdot 6H_2O$, 2 mmol $CoSO_4 \cdot 7H_2O$, 10 mL graphene solution (1 mg/mL) and 250 mg of urea were dissolved in 30 mL water and stirring for 15 min to obtain a clear solution, which was then transferred into a 50 mL Teflon-lined stainless-steel autoclave. The autoclave was locked tightly and maintained in an electric oven at 50 °C for 8h, then naturally cooled down to room temperature. The product was collected as a control.

Preparation of NiCo-HS@G/NF electrode: NiCo-HS@G/NF electrode was prepared by coating NiCo-HS@G ink on nickel foam (NF) via an ultrasonic spray-deposition setup (Sunlaite SP201, China). First, 30 mg NiCo-HS@G were ultrasonically dispersed in 20 mL ethanol for 1 h, followed by adding 20 μL 5% Nafion solution and ultrasonicating for another 0.5 h to achieve the catalyst ink. The as-prepared ink was spray-deposited on a clean NF with a catalyst loading of 1.5 mg cm^{-2}.

Preparation of NiMo/NiCo-HS@G/NF HER electrode: NiMo were electrodeposited onto NiCo-HS@G/NF working electrode using Ag/AgCl as reference electrode and carbon rod as counter electrode, similar to our previous report.[66] The deposition solution consisted of 3.52 g of sodium citrate, 1.92 g of sodium molybdate, and 3.16 g of nickel sulfate in 80 mL water with addition of 4

mL ammonia aqueous. The deposition process was proceeded at a fixed current density of -80 mA cm^{-2} for 20 min.

Material Characterization: Powder X-ray diffraction patterns were recorded on an X-ray diffraction (Rigaku D/max 2500) with a Cu Kα radiation (λ = 1.54056 Å), a generator voltage of 40 kV and current of 200 mA at a scan rate of 2° per minute in the 2 theta degree range from 5° to 80°. Morphology and structure of the materials were characterized using a SEM (Hitachi SU-8020) operating at an accelerating voltage of 15 kV and a TEM (JEOL, JEM-2100F) working at an acceleration voltage of 200 kV. The Energy dispersive spectra (EDS) were collected using EDS system (Oxford Materials Analysis) equipped on SEM and TEM. X-ray photoelectron spectroscopy (XPS) measurements were performed to determine the chemical bonding states using a Thermo Scientific ESCALab 250Xi with 300 W monochromatic Al Kα radiation. The BET isotherms were evaluated using a nitrogen adsorption-desorption apparatus (NOVA 4200e, Quantachrome, America). BET specific surface area was calculated using adsorption data in a relative pressure range from P/P_0 = 0.05-0.3. Pore size distribution was derived from the adsorption branch using the BJH method.

Electrochemical Measurements: All electrocatalytic evaluations of the catalysts were performed on an Autolab PGSTAT302N (Metrohm, Netherlands) electrochemical workstation at room temperature (25 °C) in 1 M KOH solution using a conventional three-electrode configuration. To prepare the working electrode, 3 mg of catalyst was dispersed in 500 μL of ethanol with the assistance of ultrasonication for 1 h to form a homogeneous catalyst ink. Afterwards, 25 μL of ink and 0.5 μL of 0.5% Nafion solution were drop-casted onto a glass carbon electrode with an area of 0.1256 cm^{-2} and dried in air, giving a catalyst loading of 0.12 mg cm^{-2}. The double-layer capacitances (C_{dl}) for the catalysts were measured in the potential range without Faradic process at various scan rates including 16, 14, 12, 10, 8, 6, 4 mV s^{-1}. Electrochemical impedance spectroscopy (EIS) measurements were

conducted under the potential of 0.32 V (*vs*. RHE) in the frequency range of 100 kHz to 10 mHz. Linear sweep voltammetry (LSV) polarization curves were recorded at a scan rate of 5 mV/s with 90% iR-compensation unless specifically indicated. Chronopotentiometry (CP) curves were recorded at a constant current density of 10 mA cm^{-2} without iR-compensation. Cyclic voltammograms (CVs) were conducted at a scan rate of 50 mV/s. All potentials reported in this work were referred to the reversible hydrogen electrode (RHE), which were converted according to the following equation:

$$E_{RHE} = E_{Hg/HgO} + 0.098 + 0.059 \times pH$$

Where $E_{Hg/HgO}$ is the measured potential referring to the Hg/HgO reference electrode.

The Overpotential (η) was calculated according to the following formula:

$$\eta\ (V) = E_{RHE} - 1.23\ V$$

The electrochemically active surface area (ECSA) of a catalyst was calculated via dividing C_{dl} by its specific capacitance according to the following equation:

$$ECSA = \frac{C_{dl}}{C_s}$$

Where C_s is the specific capacitance and its value was reported to be between 0.022 to 0.130 mF cm^{-2} in alkaline solution. In this work, 0.040 mF cm^{-2} was adopted as the value of C_s based on previously reported Co-based OER catalysts.[74] The roughness factor (RF) was calculated via dividing ECSA by the geometric area of the electrode (0.1256 cm^{-2}).

Four-probe resistance measurements: The powder sample was pressed into a disk at 4 MPa with two stainless-steel plungers. The resistance was measured by a Keithley 2400 digital multimeter in four-wire mode. The conductivity of a sample was then calculated according to the resistance and the size of the disk.

Calculation of Density of States (DOS): The first-principle calculations presented in this work were performed with a CASTEP program code with the plane-wave pseudopotential method.[75] We adopted the generalized gradient approximation (GGA) in the form of the Perdew-Burke-Ernzerhof for the exchange-correlation potentials.[76] Spin-polarized and LDA+U calculations were made to correctly deal with our system. The ultrasoft pseudopotential with a plane-wave energy cutoff is 380 eV. The first Brillouin zone was sampled with grid spacing of 0.024 $Å^{-1}$. The self-consistent field was set as 5×10^{-7} eV/atom. Based on the experimental lattice parameters, all independent internal atomic coordinates were optimized with the convergence standard given as follows: energy change less than 5×10^{-6} eV/atom, residual force less than 0.01 eV/Å.

Supporting Information

Supporting Information is available from the Wiley Online Library or from the author.

Acknowledgements

We acknowledge the financial support from the National Key Project on Basic Research (2015CB932302), the National Key Research and Development Program of China (2016YFB0101202), the National Natural Science Foundation of China (91645123, 21575004, 21773263, and 21573249), the Strategic Priority Research Program of the Chinese Academy of Sciences (Grant No. XDB12020100), Program for New Century Excellent Talents in University (NCET-12-0599), the National Postdoctoral Program for Innovative Talents (BX201700250), and the project sponsored by SRF for ROCS, SEM, and the Foundation for Innovation Team of Bioanalytical Chemistry of Anhui Province. We also thank the following staff scientists at the Center for Analysis and Testing, ICCAS for

their helps: Dr. Zhi-Juan Zhao, Xiao-Yu Zhang and Bao-Long Qu for XPS analysis; Yang-Sun for XRD analysis; and Dr. Bo Guan, Ji-Ling Yue and Li-Rong Liang for SEM and TEM supports.

Received: ((will be filled in by the editorial staff))
Revised: ((will be filled in by the editorial staff))
Published online: ((will be filled in by the editorial staff))

References

[1] F. Song, X. Hu, *Nat. Commun.* **2014**, *5*, 4477.

[2] B. Obama, *Science* **2017**, *355*, 126.

[3] J. Suntivich, K. J. May, H. A. Gasteiger, J. B. Goodenough, Y. Shao-Horn, *Science* **2011**, *334*, 1383.

[4] M. W. Kanan, D. G. Nocera, *Science* **2008**, *321*, 1072.

[5] R. Subbaraman, D. Tripkovic, K.-C. Chang, D. Strmcnik, A. P. Paulikas, P. Hirunsit, M. Chan, J. Greeley, V. Stamenkovic, N. M. Markovic, *Nat. Mater.* **2012**, *11*, 550.

[6] Y. Liu, H. Cheng, M. Lyu, S. Fan, Q. Liu, W. Zhang, Y. Zhi, C. Wang, C. Xiao, S. Wei, *J. Am. Chem. Soc.* **2014**, *136*, 15670.

[7] Y. Zhao, R. Nakamura, K. Kamiya, S. Nakanishi, K. Hashimoto, *Nat. Commun.* **2013**, *4*, 2390.

[8] Y. R. Zheng, M. R. Gao, Q. Gao, H. H. Li, J. Xu, Z. Y. Wu, S. H. Yu, *Small* **2015**, *11*, 182.

[9] Y. Lee, J. Suntivich, K. J. May, E. E. Perry, Y. Shao-Horn, *J. Phys. Chem. Lett.* **2012**, *3*, 399.

[10] X. Han, C. Yu, S. Zhou, C. Zhao, H. Huang, J. Yang, Z. Liu, J. Zhao, J. Qiu, *Adv. Energy Mater.* **2017**, *7*, 1602148.

[11] Z. Zhao, H. Wu, H. He, X. Xu, Y. Jin, *Adv. Funct. Mater.* **2014**, *24*, 4698.

[12] J. Huang, J. Chen, T. Yao, J. He, S. Jiang, Z. Sun, Q. Liu, W. Cheng, F. Hu, Y. Jiang, *Angew. Chem. Int. Ed.* **2015**, *54*, 8722.

[13] M. A. Sayeed, T. Herd, A. P. O'Mullane, *J. Mater. Chem. A* **2016**, *4*, 991.

[14] Y. Li, P. Hasin, Y. Wu, *Adv. Mater.* **2010**, *22*, 1926.

[15] A. Grimaud, K. J. May, C. E. Carlton, Y.-L. Lee, M. Risch, W. T. Hong, J. Zhou, Y. Shao-Horn, *Nat. Commun.* **2013**, *4*, 2439.

[16] F. Jiao, H. Frei, *Energy Environ. Sci.* **2010**, *3*, 1018.

[17] T.-L. Wee, B. D. Sherman, D. Gust, A. L. Moore, T. A. Moore, Y. Liu, J. C. Scaiano, *J. Am. Chem. Soc.* **2011**, *133*, 16742.

[18] L. Trotochaud, J. K. Ranney, K. N. Williams, S. W. Boettcher, *J. Am. Chem. Soc.* **2012**, *134*, 17253.

[19] A. Vignesh, M. Prabu, S. Shanmugam, *ACS Appl. Mater. Interfaces* **2016**, *8*, 6019.

[20] M.-R. Gao, Y.-F. Xu, J. Jiang, Y.-R. Zheng, S.-H. Yu, *J. Am. Chem. Soc.* **2012**, *134*, 2930.

[21] S. Zhao, R. Jin, H. Abroshan, C. Zeng, H. Zhang, S. D. House, E. Gottlieb, H. J. Kim, J. C. Yang, R. Jin, *J. Am. Chem. Soc.* **2017**, *139*, 1077.

[22] M.-R. Gao, X. Cao, Q. Gao, Y.-F. Xu, Y.-R. Zheng, J. Jiang, S.-H. Yu, *ACS Nano* **2014**, *8*, 3970.

[23] P. Ganesan, A. Sivanantham, S. Shanmugam, *J. Mater. Chem. A* **2016**, *4*, 16394.

[24] A. Sivanantham, S. Shanmugam, *Appl. Catal., B* **2017**, *203*, 485.

[25] B. S. Yeo, A. T. Bell, *J. Am. Chem. Soc.* **2011**, *133*, 5587.

[26] Y. Liang, Y. Li, H. Wang, J. Zhou, J. Wang, T. Regier, H. Dai, *Nat. Mater.* **2011**, *10*, 780.

[27] D. K. Zhong, J. Sun, H. Inumaru, D. R. Gamelin, *J. Am. Chem. Soc.* **2009**, *131*, 6086.

[28] Z. Chen, W. Ren, L. Gao, B. Liu, S. Pei, H.-M. Cheng, *Nat. Mater.* **2011**, *10*, 424.

[29] Y.-C. Yong, X.-C. Dong, M. B. Chan-Park, H. Song, P. Chen, *ACS Nano* **2012**, *6*, 2394.

[30] S. Chen, S.-Z. Qiao, *ACS Nano* **2013**, *7*, 10190.

[31] X.-C. Dong, H. Xu, X.-W. Wang, Y.-X. Huang, M. B. Chan-Park, H. Zhang, L.-H. Wang, W. Huang, P. Chen, *ACS Nano* **2012**, *6*, 3206.

[32] Z.-S. Wu, G. Zhou, L.-C. Yin, W. Ren, F. Li, H.-M. Cheng, *Nano Energy* **2012**, *1*, 107.

[33] R. Miao, J. He, S. Sahoo, Z. Luo, W. Zhong, S.-Y. Chen, C. Guild, T. Jafari, B. Dutta, S. A. Cetegen, *ACS Catal.* **2017**, *7*, 819.

[34] Y. Guo, L. Gan, C. Shang, E. Wang, J. Wang, *Adv. Funct. Mater.* **2017**, *27*, 1602699.

[35] D. H. Youn, Y. B. Park, J. Y. Kim, G. Magesh, Y. J. Jang, J. S. Lee, *J. Power Sources* **2015**, *294*, 437.

[36] X. Yu, M. Zhang, W. Yuan, G. Shi, *J. Mater. Chem. A* **2015**, *3*, 6921.

[37] A. Sivanantham, P. Ganesan, S. Shanmugam, *Adv. Funct. Mater.* **2016**, *26*, 4661.

[38] L. Qian, Z. Lu, T. Xu, X. Wu, Y. Tian, Y. Li, Z. Huo, X. Sun, X. Duan, *Adv. Energy Mater.* **2015**, *5*, 1500245.

[39] W. Liu, H. Liu, L. Dang, H. Zhang, X. Wu, B. Yang, Z. Li, X. Zhang, L. Lei, S. Jin, *Adv. Funct. Mater.* **2017**, *27*, 1603904.

[40] Y. Jia, L. Zhang, G. Gao, H. Chen, B. Wang, J. Zhou, M. T. Soo, M. Hong, X. Yan, G. Qian, *Adv. Mater.* **2017**, *29*, 1700017.

[41] M. A. Oliver-Tolentino, J. Vázquez-Samperio, A. Manzo-Robledo, R. D. G. Gonzalez-Huerta, J. L. Flores-Moreno, D. Ramírez-Rosales, A. Guzmán-Vargas, *J. Phys. Chem. C* **2014**, *118*, 22432.

[42] L. Qian, Z. Lu, T. Xu, X. Wu, Y. Tian, Y. Li, Z. Huo, X. Sun, X. Duan, *Adv. Energy Mater.* **2015**, *5*, 1500245.

[43] J. Duan, S. Chen, B. A. Chambers, G. G. Andersson, S. Z. Qiao, *Adv. Mater.* **2015**, *27*, 4234.

[44] C. C. McCrory, S. Jung, I. M. Ferrer, S. M. Chatman, J. C. Peters, T. F. Jaramillo, *J. Am. Chem. Soc.* **2015**, *137*, 4347.

[45] T. Tang, W.-J. Jiang, S. Niu, N. Liu, H. Luo, Y.-Y. Chen, S.-F. Jin, F. Gao, L.-J. Wan, J.-S. Hu, *J. Am. Chem. Soc.* **2017**, *139*, 8320.

[46] M. Gao, W. Sheng, Z. Zhuang, Q. Fang, S. Gu, J. Jiang, Y. Yan, *J. Am. Chem. Soc.* **2014**, *136*, 7077.

[47] J. Xie, X. Zhang, H. Zhang, J. Zhang, S. Li, R. Wang, B. Pan, Y. Xie, *Adv. Mater.* **2017**, *29*, 1604765.

[48] Q. Yang, T. Li, Z. Lu, X. Sun, J. Liu, *Nanoscale* **2014**, *6*, 11789.

[49] W. Zhang, J. Qi, K. Liu, R. Cao, *Adv. Energy Mater.* **2016**, *6*, 1502489.

[50] J. Jiang, J. Zhu, R. Ding, Y. Li, F. Wu, J. Liu, X. Huang, *J. Mater. Chem.* **2011**, *21*, 15969.

[51] C. Xia, Q. Jiang, C. Zhao, M. N. Hedhili, H. N. Alshareef, *Adv. Mater.* **2016**, *28*, 77.

[52] A.-L. Wang, H. Xu, G.-R. Li, *ACS Energy Lett.* **2016**, *1*, 445.

[53] Z. Wen, Q. Wang, Q. Zhang, J. Li, *Adv. Funct. Mater.* **2007**, *17*, 2772.

[54] C. Yuan, X. Zhang, L. Su, B. Gao, L. Shen, *J. Mater. Chem.* **2009**, *19*, 5772.

[55] X. Lu, C. Zhao, *Nat. Commun.* **2015**, *6*, 6616.

[56] C. Tang, H. S. Wang, H. F. Wang, Q. Zhang, G. L. Tian, J. Q. Nie, F. Wei, *Adv. Mater.* **2015**, *27*, 4516.

[57] C. C. McCrory, S. Jung, J. C. Peters, T. F. Jaramillo, *J. Am. Chem. Soc.* **2013**, *135*, 16977.

[58] W.-J. Jiang, S. Niu, T. Tang, Q.-H. Zhang, X.-Z. Liu, Y. Zhang, Y.-Y. Chen, J.-H. Li, L. Gu, L.-J. Wan, J.-S. Hu, *Angew. Chem. Int. Ed.* **2017**, *56*, 6572.

[59] D. Gu, C.-J. Jia, C. Weidenthaler, H.-J. Bongard, B. Spliethoff, W. Schmidt, F. Schüth, *J. Am. Chem. Soc.* **2015**, *137*, 11407.

[60] D. Li, Y. Gong, Y. Zhang, C. Luo, W. Li, Q. Fu, C. Pan, *Sci. Rep.* **2015**, *5*, 12903.

[61] J. J. Beltrán, C. A. Barrero, A. Punnoose, *J. Phys. Chem. C* **2014**, *118*, 13203.

[62] M. Zhou, L. Cai, M. Bajdich, M. García-Melchor, H. Li, J. He, J. Wilcox, W. Wu, A. Vojvodic, X. Zheng, *ACS Catal.* **2015**, *5*, 4485.

[63] M. A. Sayeed, T. Herd, A. P. O'Mullane, *J. Mater. Chem. A* **2016**, *4*, 991.

[64] M. S. Burke, M. G. Kast, L. Trotochaud, A. M. Smith, S. W. Boettcher, *J. Am. Chem. Soc.* **2015**, *137*, 3638.

[65] S. Zhao, Y. Wang, J. Dong, C.-T. He, H. Yin, P. An, K. Zhao, X. Zhang, C. Gao, L. Zhang, *Nature Energy* **2016**, *1*, 16184.

[66] S. Niu, W.-J. Jiang, T. Tang, Y. Zhang, J.-H. Li, J.-S. Hu, *Adv. Sci.* **2017**, *4*, 1700084.

[67] Y. Hou, M. R. Lohe, J. Zhang, S. Liu, X. Zhuang, X. Feng, *Energy Environ. Sci.* **2016**, *9*, 478.

[68] J. Luo, J.-H. Im, M. T. Mayer, M. Schreier, M. K. Nazeeruddin, N.-G. Park, S. D. Tilley, H. J. Fan, M. Grätzel, *Science* **2014**, *345*, 1593.

[69] M. Ledendecker, S. Krick Calderón, C. Papp, H.-P. Steinrück, M. Antonietti, M. Shalom, *Angew. Chem. Int. Ed.* **2015**, *54*, 12361.

[70] J. Li, M. Yan, X. Zhou, Z. Q. Huang, Z. Xia, C. R. Chang, Y. Ma, Y. Qu, *Adv. Funct. Mater.* **2016**, *26*, 6785.

[71] H. Jin, J. Wang, D. Su, Z. Wei, Z. Pang, Y. Wang, *J. Am. Chem. Soc* **2015**, *137*, 2688.

[72] B. You, N. Jiang, M. Sheng, S. Gul, J. Yano, Y. Sun, *Chem. Mater.* **2015**, *27*, 7636.

[73] X. Gao, H. Zhang, Q. Li, X. Yu, Z. Hong, X. Zhang, C. Liang, Z. Lin, *Angew. Chem. Int. Ed.* **2016**, *55*, 6290.

[74] C. C. McCrory, S. Jung, I. M. Ferrer, S. M. Chatman, J. C. Peters, T. F. Jaramillo, *J. Am. Chem. Soc* **2015**, *137*, 4347.

[75] S. J. Clark, M. D. Segall, C. J. Pickard, P. J. Hasnip, M. I. Probert, K. Refson, M. C. Payne, *Z. Kristallogr. - Cryst. Mater.* **2005**, *220*, 567.

[76] J. P. Perdew, K. Burke, M. Ernzerhof, *Phys. Rev. Lett.* **1996**, *77*, 3865.

Table of contents:

Kinetically controlled coprecipitation strategy is developed as a general cost-effective strategy to prepare sandwiched metal hydroxide/graphene nanocomposites. Nickel cobalt hydroxide nanosheets vertically assembled on graphene exhibit superior electrocatalytic activity and durability for oxygen evolution reaction, which enables the developed strategy to mass produce a variety of hydroxide/graphene nanocomposites for diverse energy applications.

Keyword: Hydroxide nanosheets, OER, Electrolysis, Electrocatalysts, Hydrogen production

Tang Tang, Wen-Jie Jiang,* Shuai Niu, Ning Liu, Hao Luo, Qiang Zhang, Wu Wen, Yu-Yun Chen, Lin-Bo Huang, Feng Gao,* Jin-Song Hu*

Kinetically Controlled Coprecipitation for General Fast Synthesis of Sandwiched Metal Hydroxide Nanosheets/Graphene Composites towards Efficient Water Splitting

ToC figure